Research Article | Vol. 27, No. 2 | 21 Jan 2019 | OPTICS EXPRESS 761
Optics EXPRESS

Exploiting defects in TiO_2 inverse opal for enhanced photoelectrochemical water splitting

ROWENA YEW,[1,6] SIVA KRISHNA KARUTURI,[1,2,7] JIAQIN LIU,[3,4] HARK HOE TAN,[1] YUCHENG WU,[4,5] AND CHENNUPATI JAGADISH[1]

[1]*Department of Electronic Materials Engineering, Research School of Physics and Engineering, The Australian National University, Canberra, ACT 2601, Australia*
[2]*Research School Engineering, The Australian National University, Canberra ACT 2601, Australia*
[3]*Institute of Industry & Equipment Technology, Hefei University of Technology, Hefei 230009, China*
[4]*Key Laboratory of Advanced Functional Materials and Devices of Anhui Province, Hefei 230009, China*
[5]*School of Materials Science and Engineering, Hefei University of Technology, Hefei 230009, China*
[6]*rowena.yew@anu.edu.au*
[7]*siva.karuturi@anu.edu.au*

Abstract: In this work, we report on defects generation in TiO_2 inverse opal (IO) nanostructures by electrochemical reduction in order to increase photocatalytic activity and improve photoelectrochemical (PEC) water splitting performance. Macroporous structures, such as inverse opals, have attracted a lot of attention for energy-related applications because of their large surface area, interconnected pores, and ability to enhance light-matter interaction. Photocurrent density of electrochemically reduced TiO_2-IO increased by almost 4 times, compared to pristine TiO_2-IO photoelectrodes. Raman spectroscopy and X-ray photoelectron spectroscopy (XPS) analyses confirm the presence of oxygen vacancies in electrochemically reduced TiO_2-IO photoelectrodes. Oxygen vacancies extend the absorption of TiO_2 from the UV to visible region. The incident photon-to-current efficiency (IPCE) increased by almost 3 times in the absorption (UV) region of TiO_2 and slightly in the visible region. Impedance studies show improved electrical conductivity, longer photogenerated electron lifetime, and a negative shift of the flatband potential, which are attributed to oxygen vacancies acting as electron donors. The Fermi level shifts to be closer to the conduction band edge of TiO_2-IO.

1. Introduction

PEC water splitting is considered an attractive means of harvesting solar energy and producing storable chemical fuels such as hydrogen. A photoelectrode is critical to the light harvesting and conversion efficiency of a PEC cell, wherein incident photons are absorbed, electron–hole pairs are generated, and subsequent charge transfer and catalytic conversion occurs. Particularly, photoelectrodes with nanostructured morphology contribute greatly towards the performance of PEC solar energy conversion [1,2]. TiO_2 has been widely studied as a photoanode for PEC water splitting [3] because its band-edge positions are favorable for redox reactions in water, it is chemically stable, resistant to photocorrosion, non-toxic, earth abundant and inexpensive. However, the photo-conversion efficiency of TiO_2 remains limited due to the following reasons:- Ti being a transition metal, has empty d orbitals, and its valence band being strongly influenced by oxygen 2p orbitals, results in a large bandgap of 3.0 eV (rutile) ~3.2 eV (anatase), which only allows TiO_2 to absorb in the UV region of the solar spectrum [4]. For photocatalysis, anatase TiO_2 is more reactive than the rutile phase, due to the former's longer electron lifetime; while anatase TiO_2 does have a short minority carrier lifetime, which would increase the electron-hole recombination [5]. We can overcome

#351959 https://doi.org/10.1364/OE.27.000761
Journal © 2019 Received 16 Nov 2018; revised 27 Dec 2018; accepted 27 Dec 2018; published 9 Jan 2019

Optics EXPRESS

some of these limitations by generating defects to improve photoconversion efficiency and increasing the surface area to enhance charge carrier diffusion pathways. Introduction of disorder in the lattice would enhance visible and infrared absorption with the additional benefit of carrier trapping which localises photogenerated charge carriers to prevent fast recombination. Introducing lattice disorder in TiO_2 would give rise to mid-gap states such as Ti^{3+} and oxygen vacancies. Higher mid-gap states (~3.0 eV) are derived from Ti 3d orbitals only, while the lower energy (~1.8 eV) are hybridized from both O 2p orbitals and Ti 3d orbitals, and mainly from the valence band states. Lower energy mid-gap states lie below the Fermi level and can account for a large red shift of the valence band edge. Optical transition between mid-gap states and the conduction band tail would produce a charge transfer from the O 2p orbital to the Ti 3d orbital [6]. The localization of both photoexcited electrons and holes prevents fast recombination and facilitate photogenerated carriers to the active sites to perform redox reactions [7]. There are various methods of generating defects such as plasma-treatment, high energy bombardment, thermal treatment in vacuum and thermal treatment in hydrogen environment, with last two methods being the most commonly used. Hydrogen treatment by exposing TiO_2 in hydrogen atmosphere is a widely used technique to introduce defects. Modifications of this technique by varying the temperature, pressure condition, and introducing hydrogen during the growth process by rf-sputtering has recently been explored for nanocrystals, nanostructures and nanotubes [8–11]. However, this technique requires the use of large amount of hydrogen, which makes the purpose of using TiO_2 to generate hydrogen for energy related applications counterproductive. Electrochemical reduction is a simple and cost-effective method to introduce defects into TiO_2. By applying an electric field, electrons would be driven into the TiO_2 lattice and reduces Ti^{4+} to Ti^{3+}. Recently, this method has been employed to generate defects in nanostructures such as nanotubes, nanograss and nanorods [12–14].

A nanostructured electrode possesses several favorable intrinsic characteristics for efficient light harvesting, such as access to a greater surface area, direct charge transfer pathways for reduced charge recombination, and strong light-trapping ability that promotes light harvesting by confining light within the photoelectrode. Therefore, the research community has placed enormous efforts towards the development of nanostructured semiconductor photoelectrodes for PEC solar energy conversion applications [15,16]. A photocatalyst with ordered macroporous structure can enhance molecular diffusion kinetics through its interconnected pores, as well as increase the surface area and amount of adsorption and reactive sites. Multiple reflections and scatterings inside the materials' pores may effectively extend the optical path length of incident photons within the pore network and improve light capture [17,18]. Among the various approaches to make such macroporous nanostructured materials, the template-assisted method offers a simple and versatile route to produce nanostructured materials with predefined morphology and optoelectronic properties. Due to their highly ordered and tunable porous structures, self-assembled opals have become widely popular as candidates for nanostructure fabrication [19–21].

In this work, we report the generation of defects by electrochemical reduction (ER) of TiO_2 inverse opal (IO) photoelectrodes to increase photocatalytic activity and improve PEC water splitting performance. TiO_2-IO photoelectrodes were electrochemically reduced from 300 to 500 seconds, with the photoelectrode reduced for 400 seconds (ER400s) showing the highest current density compared to pristine TiO_2-IO. The defects generated have been shown to be in the form of oxygen vacancies, which shifts the Fermi level towards the conduction band edge, thus improving the conductivity of the TiO_2-IO electrode.

2. Experimental

TiO_2-IOs were fabricated by using the evaporation-assisted self-assembly via vertical deposition method with polystyrene (PS) particles as a sacrificial template on fluorine-doped SnO_2 (FTO) coated glass substrates. FTO substrates were first ultrasonically cleaned in

Optics EXPRESS

ethanol for 1 hour before being dipped in a mixed suspension of Thermo Scientific carboxylate modified polystyrene particles of 530 nm in diameter and deionized water in the proportion of 0.15 wt%. FTO substrates dipped in the mixture were placed in an oven for approximately 22 hours, allowing lateral capillary forces to deposit PS particles on the substrate as water evaporated. The infiltration of sacrificial PS template with TiO_2 was carried by atomic layer deposition (ALD), using titanium tetrachloride and deionized water as sources for Ti and O respectively in a Picosun R200 ALD system at 85°C. Annealing the infiltrated opal templates at 450° C for 30 mins in air converted them from amorphous phase to crystalline phase and remove the PS sacrificial template, leaving behind anatase TiO_2-IO. Samco ICP-RIE (RIE-4100iP) was used to etch the top layer of TiO_2-IO to allow electrolyte to infiltrate deep into the porous structure.

Electrochemical reduction of TiO_2 inverse opals was carried by an anodic reduction process using a two-electrode configuration and a potentiostat (Autolab, PGSTAT302N) setup, with TiO_2-IO as the working electrode and Pt wire as the counter electrode. With the two photoelectrodes placed approximately 2.5 cm apart, electrochemical reduction was carried at a voltage of – 3V from 300 to 600 seconds in an electrolyte bath of 0.5 M Na_2SO_4. After the anodic reduction, the samples were rinsed in deionized water and dried with nitrogen.

The surface morphology and structure were characterized by scanning electron microscopy (SEM, FEI Helios Nanolab 600) operating at a voltage of 3 kV. Phase identification of TiO_2 was carried out by grazing incidence X-ray diffraction (GIXRD, PANanalytical), using Cu-Kα radiation (λ = 1.54 angstrom) with a voltage of 45 kV from 20° to 80°. Raman spectroscopy (Renishaw) using a 532 nm laser with Raman shift from 100 to 800 cm^{-1}, was carried out to confirm the defects generated from the electrochemical reduction process. X-ray photoelectron spectroscopy (XPS) using monochromated Al K alpha x-ray source (energy 1486.68 eV) and ultra-violet photoelectron spectroscopy (UPS) using with a He(I) beam (21.1 eV) was performed with Thermo Scientific ESCALAD 250Xi. Diffuse reflectance and transmittance were measured using a Perkin Elmer UV-Vis spectrophotometer equipped with an integrating sphere.

PEC performance, electrochemical impedance spectroscopy (EIS) and Mott-Schottky analyses of the photoanodes were evaluated in a three-electrode PEC cell configuration using a potentiostat (Autolab, PGSTAT302N). All potentials were reported against the reversible hydrogen electrode (RHE) using Nernst's equation E (V_{RHE}) = E ($V_{Ag/AgCl}$) + 0.059 pH + 0.197. Ag/AgCl in saturated KCl and a Pt wire were used as reference and counter electrodes, respectively in 1 M NaOH (pH = 13) as the electrolyte. Photoresponse characteristics were measured using a solar simulator (Newport) equipped with a 150 W Xe lamp and an AM 1.5G filter, calibrated with a standard Si solar cell. Transient photocurrent measurements were performed under chopped light irradiation (on-off light cycles of 50 s) at an applied bias of 1.23 V_{RHE} in 1 M NaOH. Photocurrent stability measurement was performed at an applied bias of 1.23 V_{RHE} in 1 M NaOH for a duration of 3.5 hours. Open circuit voltages for all samples were measured before EIS was performed from 10^{-2} to 10^{5} Hz at 10 mV amplitude. Mott-Schottky analyses were performed at a frequency of 500 Hz and an applied voltage of 10 mV. ZView from Scribner Associates was used to analyse EIS data. The incident-photon-to-current conversion efficiency (IPCE) measurements were taken in a three-electrode configuration as a function of wavelength from 300 to 600 nm using a 1000 W Xe lamp coupled to a monochromator. The incident light intensity was calibrated using a Thorlabs PM100D power meter and a standard silicon photodiode power sensor of wavelength range 200 – 1100 nm. IPCE was calculated according to the following equation:

$$IPCE(\%) = \left[1240\left(V.nm\right)\times j_{photo}\left(mA/\mathrm{cm}^2\right)\right]/\left[P_{mono}\left(mW/cm^2\right)\times\lambda\left(nm\right)\right]\times 100\% \quad (1)$$

Optics EXPRESS

where 1240 V.nm is the multiplication of Planck's constant and the speed of light, j_{photo} is the measured photocurrent density in mA/cm^2, P_{mono} is the calibrated and monochromated illumination power intensity in mW/cm^2 and λ (nm) is the wavelength at which this illumination power is measured.

3. Results and discussion

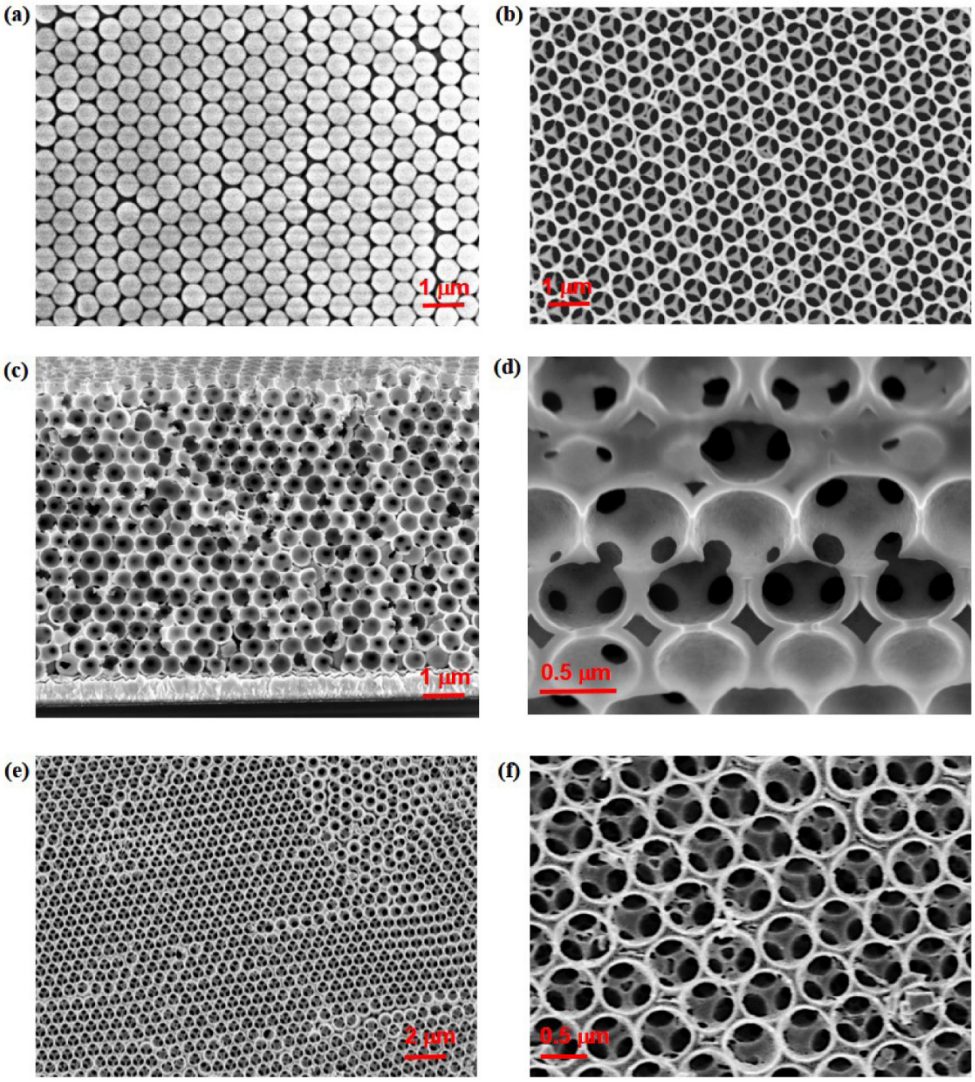

Fig. 1. SEM images of (a) PS opal template (b) top view of TiO_2-IO (c) cross section of TiO_2-IO (d) magnified cross sectional image TiO_2-IO showing the pore structure (e) ER400s-TiO_2-IO and (f) ER400s TiO_2-IO after 3.5 hrs of photoelectrochemical stability test.

Figure 1(a) shows the highly ordered PS sacrificial template consisting of a face-centered cubic array structure with PS spheres stacked in an orderly manner. By using a stop-flow ALD method, we can effectively infiltrate the PS sacrificial template to achieve uniform and high filling fraction of the macroporous structure with an average pore size of approximately 500 ± 10 nm as seen in Figs. 1(b) and 1(c). The magnified cross-section of TiO_2-IO in Fig. 1(d) shows a well-connected macroporous structure with unclogged and well-defined pore

Optics EXPRESS

openings. This would allow infiltration of the electrolyte deep into the structure ensuring shorter pathways for photogenerated carriers. Photogenerated holes can easily reach reactive sites to perform the oxidation process, while photogenerated electrons can travel quickly to the FTO ohmic contact, through the cell and to the counter electrode to perform the reduction process. Recombination of electron-hole pairs is reduced since photogenerated carriers can access their respective sites quickly. After undergoing electrochemical reduction and stability test for 3.5 hours, the TiO_2-IO maintains its structure and the pores remained unclogged, as shown in Figs. 1(e) and 1(f).

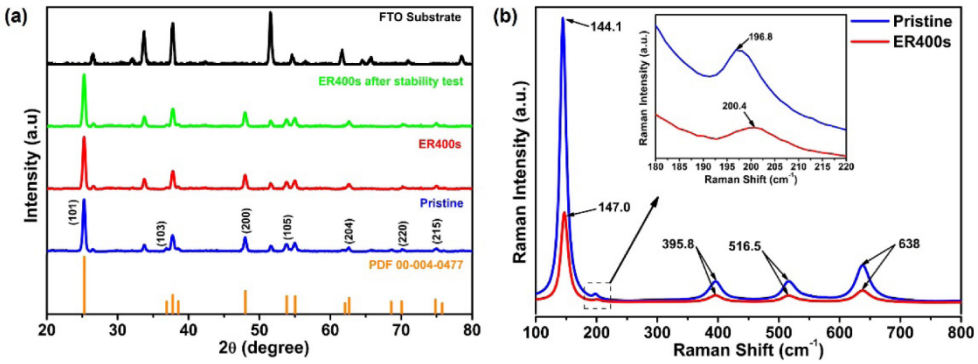

Fig. 2. (a) XRD patterns of FTO substrate, pristine, ER400s and ER400s (after stability test) TiO_2-IO (b) Raman spectra of pristine and ER400s TiO_2-IOs.

The crystalline structure of both pristine and ER TiO_2-IO was characterized by GIXRD as shown in Fig. 2(a). The major XRD peaks at 25.23°, 36.84°, 48°, 53.65°, 62.53°, 70.37°, and 75° with d_{hkl} 3.51, 2.44, 1.89, 1.70, 1.48, 1.34 and 1.26 $\dot{A}$ can be indexed to the tetragonal anatase phase of TiO_2 (PDF card no. 00-044-0477). These peaks correspond to the diffraction planes (101), (103), (200), (105), (204), (220) and (215) respectively. There is no change in the phase after the electrochemical reduction process and after 3.5 hours of photoelectrochemical stability test. The Raman spectrum as seen in Fig. 2(b) for pristine TiO_2-IO shows six active modes with three E_g modes at 144.1 cm^{-1}, 196.8 cm^{-1} and 637.2 cm^{-1}; two B_{1g} modes at 395 cm^{-1} and 516.5 cm^{-1}; and one A_{1g} mode at 516.5 cm^{-1}. These modes are typical of anatase TiO_2 [22]. The active mode E_g is caused by symmetric stretching vibration, B_{1g} by the symmetric bending and A_{1g} by the antisymmetric bending of O-Ti-O in TiO_2 [23]. Both the $E_g(1)$ and $E_g(2)$ modes at 144.1 cm^{-1} and 196.8 cm^{-1} from ER400s TiO_2-IO are blue-shifted, while the rest of the Raman modes remain unchanged. These two peak shifts have been attributed to lattice disorder resulting from a phonon confinement effect or a stoichiometric change [24]. From the XRD pattern and using Scherrer's equation, the crystallite size of both pristine and reduced TiO_2 was estimated to be 22 nm. Phonon confinement effect can be ruled out since there was no change in grain size of the pristine and ER400s TiO_2-IO; and only the E_g modes were shifted. Removing an oxygen atom from the TiO_2 lattice forces the three Ti atoms to shorten their overlapping dangling bonds with each other and strengthen their bonds with the rest of the lattice, thus decreasing the Ti-O bond length [25]. This reduction in the bond length is reflected in the shift of E_g modes to a higher wave number, since the E_g modes are mainly caused by the symmetric stretching of the Ti-O bond and is sensitive to change in bond length. All the peaks of the ER400s broadened, as compared to the pristine sample, with full width half maximum (FWHM), shown in Table 1. Peak broadening can be attributed to the excess oxygen vacancies leading to non-stoichiometry of TiO_2 [26]. Thus, the peak shift, broadening of the peaks and decrease in intensity of surface structure of TiO_2 are due to the defects, in this case oxygen vacancies generated from the reduction process [27].

Optics EXPRESS

Table 1. FWHM of Raman spectra for pristine and ER400s samples

	Pristine		ER400s	
Mode	**Wavenumber (cm^{-1})**	**FWHM (cm^{-1})**	**Wavenumber (cm^{-1})**	**FWHM (cm^{-1})**
Eg	144.1	12.8	147	14.41
B1g	395.8	29.87	395.8	31.52
A1g + B1g	516.5	33.14	516.5	37.33
Eg	638	29.62	638	33.81

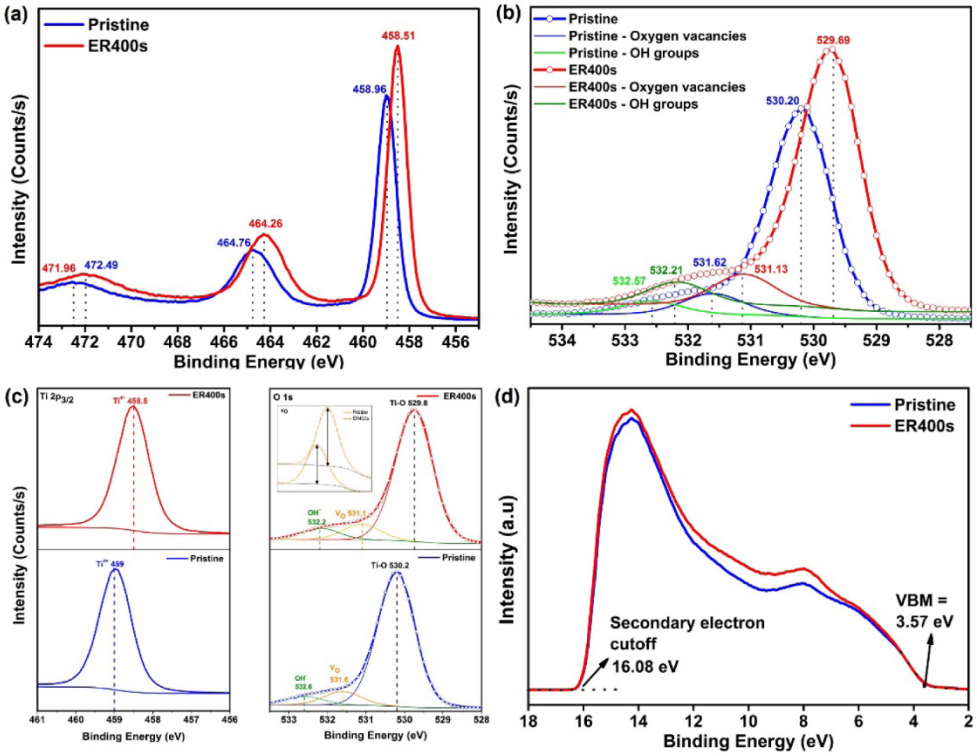

Fig. 3. (a) XPS core level spectra of Ti 2p (b) XPS core level spectra of O 1s (c) Fitting of XPS core level spectra (d) UPS spectra of pristine and ER400s TiO_2-IOs.

XPS analysis was carried out to determine the chemical environment and type of surface defects induced by the reduction process. For the XPS core-level spectra of Ti 2p in Fig. 3(a), the peaks at binding energy (BE) 459 eV for pristine and 458.5 eV for ER TiO_2-IO have been assigned to Ti^{4+} species. No peaks for Ti^{3+} species have been observed hence suggesting there was no reduction of Ti^{4+} to Ti^{3+} [28,29]. The spectra of O 1s in Fig. 3(b) has one main peak at BE 530.2 eV (pristine) and 529.8 eV (ER TiO_2-IO) characteristic of Ti-O. The two smaller shoulder peaks are assigned to the surface oxygen vacancies, with BE 531.6 eV (pristine) and 531.1 eV (ER) TiO_2-IO; and the surface OH group with BE 532.6 eV (pristine) and 532.2 eV (ER) TiO_2-IO as shown in Fig. 3(c). With the reduction process, there is a decrease in atomic percentages in Ti^{4+} and Ti-O peaks while an increase in the peaks is attributed to oxygen vacancies and the OH group, shown in the inset of Fig. 3(c). A shift to lower binding energies of both O 1s and Ti 2p spectra of ER-TiO_2 is observed across all the peaks. A lack of Ti^{3+} in ER TiO_2-IO with a shift to lower BE in the spectra indicates that electrons bound to the oxygen and titanium ions migrated to the oxygen vacancies; with the

Optics EXPRESS

latter serving as electron traps. The shift in O 1s spectra can be attributed to the transfer of electrons to the neighbouring oxygen vacancies [30–32].

UPS measurements were performed to determine the valence band maximum and the work function of TiO_2-IOs before and after the reduction process. The reduction of TiO_2-IOs did not change the valence band maximum which is 3.57 eV below the Fermi level as indicated in Fig. 3(d). The work function of a semiconductor surface is given by $\phi_s = h\upsilon - E_{sc}$ where $h\upsilon$ is the energy of photons emitted by helium gas of 21.2 eV and E_{sc} is the secondary electron cut-off. The work function for both samples is 5.12 eV, which agrees with reported values for polycrystalline anatase TiO_2 [33]. However, there is an increase in the peak intensity due to the increase in oxygen vacancies from the reduction process.

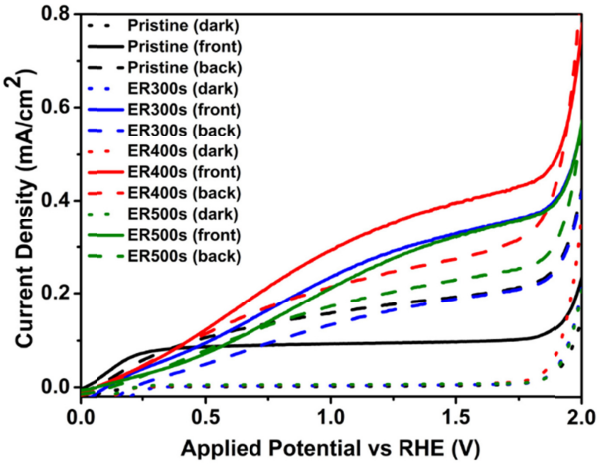

Fig. 4. Linear sweep voltammograms obtained for pristine and electrochemically reduced TiO_2-IO photoelectrodes for duration of 300 s, 400 s and 500 s in 1 M NaOH (pH = 13) electrolyte, in darkness and under AM1.5 G simulated sunlight (100 mW cm^{-2}), and at a scan rate of 10 mV s^{-1}.

Figure 4 shows the linear sweep voltammetry (LSV) of pristine and ER TiO_2-IO photoelectrodes illuminated through the front and back side. Pristine TiO_2-IO photoelectrode has a current density of 0.09 mA/cm^2 (front side illumination) and 0.18 mA/cm^2 (back side illumination) with an applied potential of 1.23 V_{RHE}, while electrochemically reduced for 400s (ER400s) TiO_2-IO photoelectrode has the highest current density of 0.35 mA/cm^2 (front side illumination) with an applied potential of 1.23 V_{RHE}. When pristine TiO_2-IO photoelectrode was illuminated from the front, the Fermi level downshift towards the conduction band and surface state assisted recombination decreases leading to an initial photoanodic current increase. However, as the surface states are filled with photogenerated holes, the photoanodic current starts to plateau which corresponds to the maximum achievable current from the surface states. The photocurrent saturates once the surface states assisted recombination have been eliminated by electrons. When ER400s TiO_2-IO photoelectrode was illuminated from front and back side, we see only an increasing photoanodic current until saturation is reached.

For an n-type semiconductor such as TiO_2, photogenerated holes migrate to the semiconductor-electrolyte interface (SEI), while photogenerated electrons travel to the FTO ohmic contact. Absorption of photons and generation of carriers occur at the surface where they are illuminated. Direction and distance travelled by photogenerated carriers are the same regardless of direction of illumination. However, the photocurrent is dependent on the direction of illumination and can indicate the limitations of electron or hole transport. The fact that photocurrent generated is significantly different for pristine and ER400s TiO_2-IO

Optics EXPRESS

photoelectrodes confirms that the charge recombination is significant in pristine TiO_2-IO. This is addressed by introducing oxygen vacancies in TiO_2-IO. Oxygen vacancies not only act as electron donors thus lowering the Fermi level towards the conduction band, they also serve as electron traps to prevent charge recombination. Since the depletion layer width is dependent on the donor density, oxygen vacancies present in the TiO_2 lattice can affect the depletion layer width [34]. With increased oxygen vacancies generated by the electrochemical reduction process, the depletion layer width is shortened, recombination is reduced, thus improving charge carrier migration to their respective sites. However, increasing the reduction time from 400 s to 500 s leads to a decrease in photocurrent density, which can be attributed to the excessive generation of oxygen vacancies. With excess oxygen vacancies, more electrons are trapped thus lowering density of electrons collected at the FTO ohmic contact.

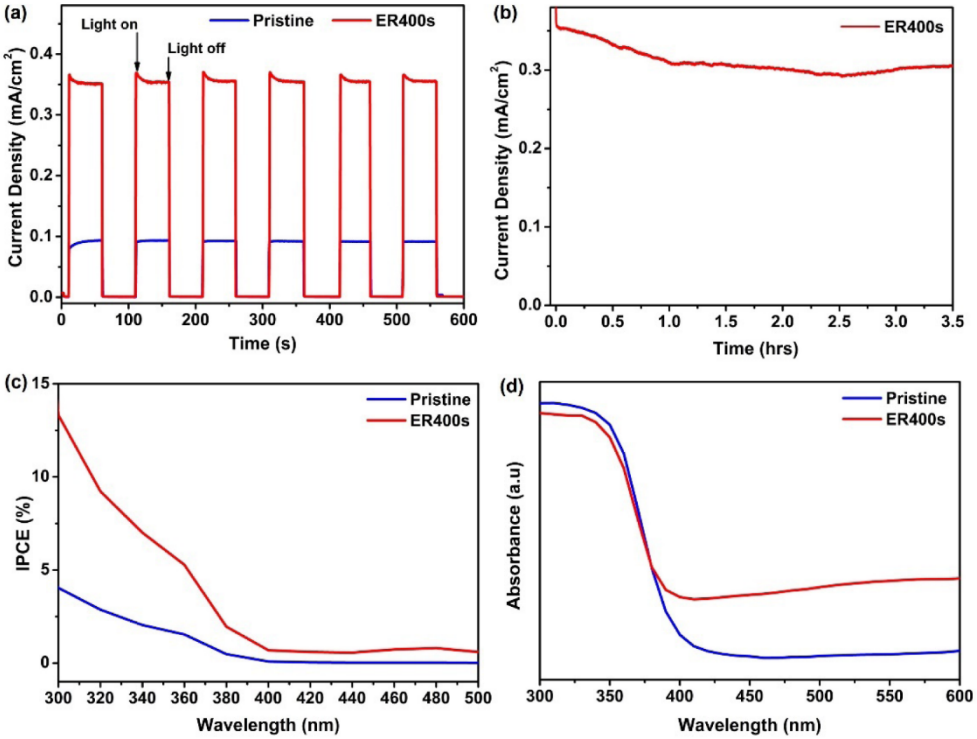

Fig. 5. (a) Transient photocurrent responses of pristine and ER400s TiO_2-IO photoelectrodes measured under 50 s on-off light cycles (b) Photocurrent-time measurement of ER400s TiO_2-IO photoelectrode measured for 3.5 hours (c) IPCE of pristine and ER400s TiO_2-IO photoelectrodes measured at incident wavelength from 300 to 500 nm and (d) absorption spectra of pristine and ER400s TiO_2-IO photoelectrodes as a function of wavelength. Transient photocurrent, photocurrent-time and IPCE measurements were carried out in 1 M NaOH at an applied potential of 1.23 V_{RHE}.

Figure 5(a) shows the transient photocurrent responses for pristine and ER400s TiO_2-IO photoelectrodes at an applied potential of 1.23 V_{RHE} with 50 s on-off light cycles. The photocurrents for both pristine and ER400s-IO photoelectrodes reflect the measured values from LSV, and is maintained for over a period of 600 s. The transient features indicate whether recombination is limiting the charge transfer process and the type of recombination that occurs at the SEI [35]. An anodic transient would correspond to holes accumulated, while a cathodic transient corresponds to electrons being dissipated at the SEI. For the ER400s TiO_2-IO photoelectrode, an anodic photocurrent spike is observed due to the sudden

Optics EXPRESS

generation of charge carriers, which then decays to a steady-state photocurrent due to recombination processes or a decrease in band bending [36]. For pristine TiO_2-IO photoelectrode, photogenerated holes travel to the surface at a slow but sufficient rate to react with the electrolyte, thereby avoiding accumulation. By creating oxygen vacancies, electrons are trapped in the mid-gap states as well as absorption sites where hole transfer to the absorbed ionic species can prevent further recombination [37]. Long-term stability of ER400s TiO_2-IO photoelectrode was subjected to continuous AM1.5 simulated sunlight illumination for 3.5 hours. Under an applied potential of 1.23 V_{RHE}, the initial photocurrent density of 0.35 mA/cm^2 decreased by 14% to 0.29 mA/cm^2, as shown in Fig. 5(b). To quantify light absorption and photoconversion efficiencies of the TiO_2-IO photoelectrodes, we measure the incident photon-to-current efficiency (IPCE) where the photocurrents are obtained as a function of wavelength. Figure 5(c) shows the IPCE increasing almost 3 times in the absorption region of TiO_2 after electrochemical reduction, as well as increase slightly in the visible region. The increase in photoconversion efficiency of TiO_2-IO in the UV as well as in the visible regions can be attributed to the enhanced photocurrent density in ER400s TiO_2-IO photoelectrodes. The UV-Vis spectra in Fig. 5(d) shows the absorption band edges for both TiO_2-IO photoelectrodes at the wavelength of 400 nm, which is at the absorption bandgap of anatase TiO_2. The ER400s TiO_2-IO photoelectrode exhibits a strong sub-bandgap absorption from 400 nm to the infrared region due to an extended Urbach tail, which has been attributed to lattice disorder or vacancies [38].

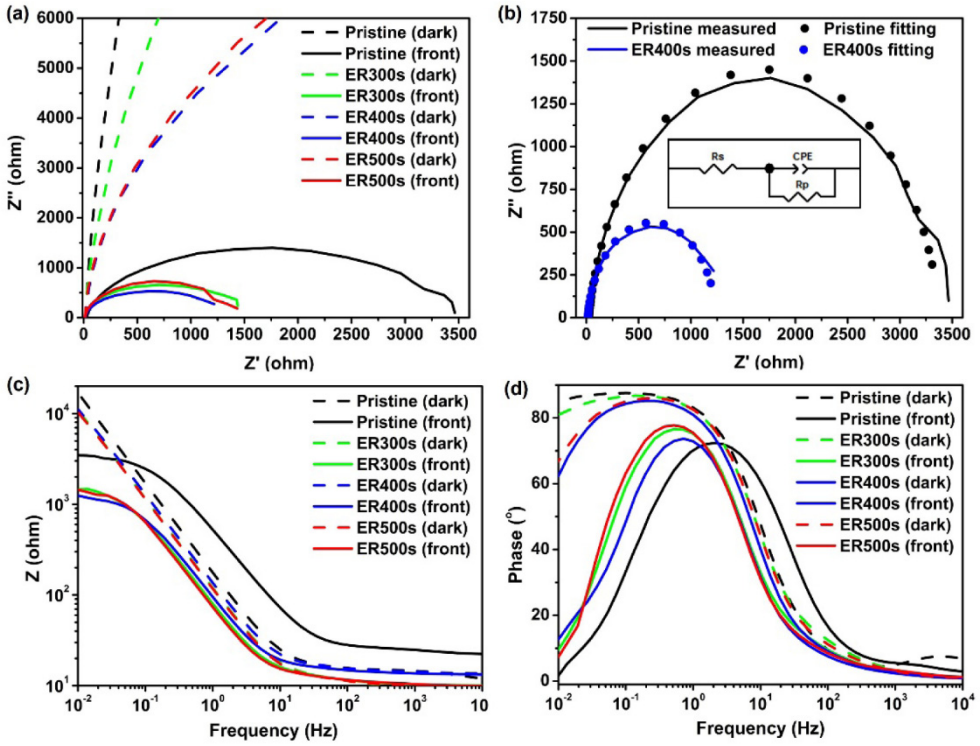

Fig. 6. (a) Nyquist plot of pristine, ER300s, ER400s and ER500s TiO_2-IO photoelectrodes (b) Nyquist plots of pristine and ER400s TiO_2-IO photoelectrodes fitted to the equivalent circuit. (c) Bode magnitude and (d) Bode phase plots of pristine, ER300s, ER400s and ER500s TiO_2-IO photoelectrodes.

EIS was used to evaluate charge transfer kinetics at the SEI by measuring the AC response of pristine and ER400s TiO_2-IO photoelectrodes. Nyquist and Bode plots of pristine

Optics EXPRESS

and ER400s TiO_2-IO photoelectrodes obtained from EIS was carried out at open-circuit potential, under dark and illuminated conditions. The internal resistances corresponding to the overall charge transfer process under illumination were significantly lower than those in dark conditions due to the generation of electron-hole pairs. In Nyquist plots, the real and negative imaginary components of the complex impedance Z are plotted on the horizontal and vertical axis, respectively. The presence of one semicircle indicates that an electrochemical interface is present in the system. In Fig. 6(a), all TiO_2-IO photoelectrodes under illumination have lower impedances than those performed in the dark indicating that photogenerated electron-hole pairs lower the resistance of the photoelectrodes. The ER400s TiO_2-IO photoelectrode has a lower impedance compared to the pristine electrode which shows that oxygen vacancies improved charge transfer kinetics at the SEI. A Randles circuit as shown in the inset of Fig. 6(b), consists of a series resistance (R_s) element followed by a parallel RC, which is a combination of parallel resistance (R_p) and a constant phase element (CPE), and is used for modeling the response of the photoelectrodes. The series resistance represents the ohmic resistance between FTO and TiO_2-IO, while the parallel resistance is associated with charge transfer from TiO_2-IO to the electrolyte, and the CPE is the impedance originating from the charge in the space charge layer in TiO_2-IO. The CPE is a fitting element with impedance of $Z_{CPE} = 1 / Q(j\omega)^{\alpha}$, and when α equals 1, 0, or − 1 a CPE behaves as a capacitor, a resistor, or an inductor. By fitting the Nyquist plots using the equivalent Randles circuit, we can ascertain the appropriate behavior of system to AC response. Through the creation of oxygen vacancies, Ti-O bonds are broken, producing excess valence electrons that are bonded to oxygen atoms in the valence band, and in migrating from a lower to higher energy level, conductivity of the electrode is improved [39]. From the Bode magnitude plots shown in Fig. 6(c), the impedance measured corresponds to R_s and R_p at low frequencies, while at higher frequencies, we see a drop in the overall impedance indicating that the charge transfer resistance at the interface has dropped since the resistance between the ohmic contact and TiO_2-IO did not change. From the frequency peaks in the Bode phase plots in Fig. 6(d), lifetime of photogenerated electrons can be calculated using, $\tau_n = 1/ (2\pi f_{max})$, where f_{max} is the maximum oscillation frequency of the impedance. Photogenerated electron lifetimes for pristine and ER400s TiO_2-IO photoelectrodes were calculated to be 75 and 234 ms respectively. By generating oxygen vacancies, electron lifetimes have been extended leading to the increase of electron diffusion length and inhibition of electron-hole recombination.

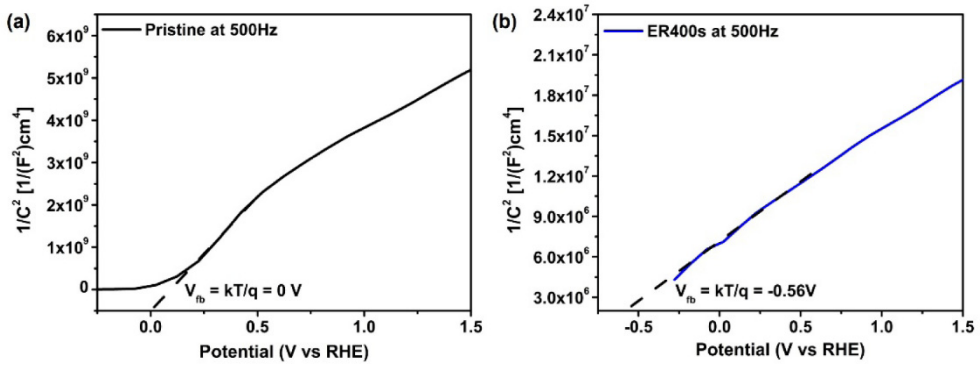

Fig. 7. (a) Mott-Schottky plots collected for (a) pristine (b) ER400s TiO_2-IO photoelectrodes at 500Hz in dark condition.

Mott-Schottky analysis for both pristine and ER400s TiO_2-IO photoelectrodes was carried to determine the flatband potential and charge carrier density, as shown in Figs. 7(a) and 7(b). The Mott-Schottky equation can be written as:

Optics EXPRESS

$$\frac{1}{C^2} = \frac{2}{\left(q\varepsilon\varepsilon_0 N_D A^2\right)}\left(E_{app} - E_{fb} - \frac{kT}{q}\right) \quad (2)$$

where C is the capacitance at the space charge layer, ε is the dielectric constant (anatase TiO_2 = 45), ε_0 is the permittivity in free space, A is the area, q is the elementary charge, N_D is the donor carrier concentration, E_{app} is the applied electrochemical potential, E_{fb} is the flatband potential, k_B is the Boltzmann constant, and T is the temperature (25°C). The x-intercept of the Mott-Schottky plot provides us the flatband potential and the slope can be used to determine the donor density. The flatband potential pristine and ER400s TiO_2-IO photoelectrodes are determined to be 0 eV (vs RHE) and − 0.56 eV (vs RHE) respectively. The flatband potential, E_{fb}, is the electrochemical potential applied to the semiconductor that reduces this band bending to zero, thus the cathodic shift of the flatband potential can lower the onset potential. The gentler slope of ER400s TiO_2-IO indicates higher donor concentration compared to that of pristine TiO_2-IO photoelectrode. The introduction of oxygen vacancies which act as electron donors, shifts the Fermi level towards the conduction band and improves conductivity, as shown in impedance studies.

4. Conclusions

Defects in TiO_2 can be generated easily and quickly by electrochemical reduction process. Electrochemically reduced TiO_2 macroporous nanostructures such as TiO_2-IO photoelectrodes show an improvement in photon absorption and PEC water splitting performance. The defects generated in these TiO_2-IO photoelectrodes are oxygen vacancies. The performance of the electrochemically reduced photoelectrodes is dependent on the reduction times, with 400 s being the optimal reduction time. Longer reduction time produces excessive oxygen vacancies that act as electron traps, thereby limiting the density of electrons collected at the FTO ohmic contact. There is an increase in the photon absorption of the ER400s TiO_2-IO photoelectrode in the visible region and photoconversion efficiency in the UV region increasing by almost 3 folds. This improved performance ostensibly results from the creation of oxygen vacancies in the TiO_2-IO photoelectrodes due to shift in Fermi level towards the conduction band, which in turn leads to lower electron-hole recombination rates and improved charge transport. However, in the experiment, the valence band did not change and the reduction of the bandgap of TiO_2-IO was not achieved. This work has shown that by introducing oxygen vacancies, we can increase photogenerated carrier lifetime and thus improve the conductivity of TiO_2 to enhance PEC water splitting performance.

Funding

Australian Research Council (ARC).

Acknowledgments

We would like to acknowledge the Australian National Fabrication Facility (ANFF), ACT Node for access to their facilities. We acknowledge the Ministry of Education of China's 111 program - Base of Introducing Talents of Discipline to Universities for Advanced Clean Energy Materials and Technology for enabling this collaboration between ANU and HFUT. We thank Prof. Jodie Bradby and Tom Shiell for access to their Raman spectrometer and the Raman measurements.

References

1. M. Grätzel, "Photoelectrochemical cells," Nature **414**(6861), 338–344 (2001).
2. M. G. Walter, E. L. Warren, J. R. McKone, S. W. Boettcher, Q. Mi, E. A. Santori, and N. S. Lewis, "Solar water splitting cells," Chem. Rev. **110**(11), 6446–6473 (2010).
3. A. Fujishima and K. Honda, "Electrochemical photolysis of water at a semiconductor electrode," Nature **238**(5358), 37–38 (1972).

Optics EXPRESS

4. T. Jafari, E. Moharreri, A. S. Amin, R. Miao, W. Song, and S. L. Suib, "Photocatalytic water splitting - the untamed dream: a review of recent advances," Molecules **21**(7), 900 (2016).
5. Y. Yamada and Y. Kanemitsu, "Determination of electron and hole lifetimes of rutile and anatase TiO_2 single crystals," Appl. Phys. Lett. **101**(13), 133907 (2012).
6. X. Chen, L. Liu, P. Y. Yu, and S. S. Mao, "Increasing solar absorption for photocatalysis with black hydrogenated titanium dioxide nanocrystals," Science **331**(6018), 746–750 (2011).
7. I. Justicia, P. Ordejón, G. Canto, J. L. Mozos, J. Fraxedas, G. A. Battiston, R. Gerbasi, and A. Figueras, "Designed self-doped titanium dioxide thin films for efficient visible-light photocatalysis," Adv. Mater. **14**(19), 1399–1402 (2002).
8. A. P. Singh, N. Kodan, B. R. Mehta, A. Dey, and S. Krishnamurthy, "In-situ plasma hydrogenated TiO_2 thin films for enhanced photoelectrochemical properties," Mater. Res. Bull. **76**, 284–291 (2016).
9. L. Han, Z. Ma, Z. Luo, G. Liu, J. Ma, and X. An, "Enhanced visible light and photocatalytic performance of TiO_2 nanotubes by hydrogenation at lower temperature," RSC Advances **6**(8), 6643–6650 (2016).
10. M. Mehta, N. Kodan, S. Kumar, A. Kaushal, L. Mayrhofer, M. Walter, M. Moseler, A. Dey, S. Krishnamurthy, S. Basu, and A. P. Singh, "Hydrogen treated anatase TiO_2: a new experimental approach and further insights from theory," J. Mater. Chem. A Mater. Energy Sustain. **4**(7), 2670–2681 (2016).
11. D. K. Behara, A. K. Ummireddi, V. Aragonda, P. K. Gupta, R. G. Pala, and S. Sivakumar, "Coupled optical absorption, charge carrier separation, and surface electrochemistry in surface disordered/hydrogenated TiO_2 for enhanced PEC water splitting reaction," Phys. Chem. Chem. Phys. **18**(12), 8364–8377 (2016).
12. Z. Zhang, M. N. Hedhili, H. Zhu, and P. Wang, "Electrochemical reduction induced self-doping of Ti^{3+} for efficient water splitting performance on TiO_2 based photoelectrodes," Phys. Chem. Chem. Phys. **15**(37), 15637–15644 (2013).
13. P. Yan, G. Liu, C. Ding, H. Han, J. Shi, Y. Gan, and C. Li, "Photoelectrochemical water splitting promoted with a disordered surface layer created by electrochemical reduction," ACS Appl. Mater. Interfaces **7**(6), 3791–3796 (2015).
14. J.-W. Yun, K. Y. Ryu, T. K. Nguyen, F. Ullah, Y. Chang Park, and Y. S. Kim, "Tuning optical band gap by electrochemical reduction in TiO_2 nanorods for improving photocatalytic activities," RSC Advances **7**(11), 6202–6208 (2017).
15. H. M. Chen, C. K. Chen, R. S. Liu, L. Zhang, J. Zhang, and D. P. Wilkinson, "Nano-architecture and material designs for water splitting photoelectrodes," Chem. Soc. Rev. **41**(17), 5654–5671 (2012).
16. R. van de Krol, Y. Liang, and J. Schoonman, "Solar hydrogen production with nanostructured metal oxides," J. Mater. Chem. **18**(20), 2311–2320 (2008).
17. S. K. Karuturi, C. Cheng, L. Liu, L. Tat Su, H. J. Fan, and A. I. Y. Tok, "Inverse opals coupled with nanowires as photoelectrochemical anode," Nano Energy **1**(2), 322–327 (2012).
18. S. K. Karuturi, J. Luo, C. Cheng, L. Liu, L. T. Su, A. I. Y. Tok, and H. J. Fan, "A novel photoanode with three-dimensionally, hierarchically ordered nanobushes for highly efficient photoelectrochemical cells," Adv. Mater. **24**(30), 4157–4162 (2012).
19. C. Cheng, S. K. Karuturi, L. Liu, J. Liu, H. Li, L. T. Su, A. I. Y. Tok, and H. J. Fan, "Quantum-dot-sensitized TiO_2 inverse opals for photoelectrochemical hydrogen generation," Small **8**(1), 37–42 (2012).
20. R. Yew, S. K. Karuturi, H. H. Tan, and C. Jagadish, *Semiconductors and Semimetals – Semiconductors for Photocatalysis* (Elsevier, 2017), Chap. 8.
21. S. K. Karuturi, R. Yew, P. R. Narangari, J. Wong-Leung, L. Li, K. Vora, H. H. Tan, and C. Jagadish, "CdS / TiO_2 photoanodes via solution ion transfer method for highly efficient solar hydrogen generation," Nano Futures **2**(1), 015004 (2018).
22. T. Ohsaka, F. Izumi, and Y. Fujiki, "Raman spectrum of anatase TiO_2," J. Raman Spectrosc. **7**(6), 321–324 (1978).
23. F. Tian, Y. Zhang, J. Zhang, and C. Pan, "Raman spectroscopy : a new approach to measure the percentage of anatase TiO_2 exposed (001) facets," J. Phys. Chem. C **116**(13), 7515–7519 (2012).
24. D. Bersani, P. P. Lottici, and X. Ding, "Phonon confinement effects in the Raman scattering by TiO_2 nanocrystals phonon confinement effects in the Raman scattering by TiO_2 nanocrystals," Appl. Phys. Lett. **73**(1), 72–75 (1998).
25. A. Janotti, J. B. Varley, P. Rinke, N. Umezawa, G. Kresse, and C. G. Van de Walle, "Hybrid functional studies of the oxygen vacancy in TiO_2," Phys. Rev. B Condens. Matter Mater. Phys. **81**(8), 085212 (2010).
26. J. C. Parker and R. W. Siegel, "Raman microprobe study of nanophase TiO_2 and oxidation-induced spectral changes," J. Mater. Res. **5**(6), 1246–1252 (1990).
27. S. Sahoo, A. K. Arora, and V. Sridharan, "Raman line shapes of optical phonons of different symmetries in anatase TiO_2 nanocrystals," J. Phys. Chem. C **113**(39), 16927–16933 (2009).
28. C. M. Greenlief, J. M. White, C. S. Ko, and R. J. Gorte, "An XPS investigation of titanium dioxide thin films on polycrystalline platinum," J. Phys. Chem. **89**(23), 5025–5028 (1985).
29. M. C. Biesinger, L. W. Lau, A. R. Gerson, and R. S. Smart, "Resolving surface chemical states in XPS analysis of first row transition metals, oxides and hydroxides: Sc, Ti, V, Cu and Zn," Appl. Surf. Sci. **257**(3), 887–898 (2010).
30. K. Du, G. Liu, M. Li, C. Wu, X. Chen, and K. Wang, "Electrochemical reduction and capacitance of hybrid titanium dioxides - nanotube arrays and nanograss," Electrochim. Acta **210**, 367–374 (2016).
31. A. C. Papageorgiou, N. S. Beglitis, C. L. Pang, G. Teobaldi, G. Cabailh, Q. Chen, A. J. Fisher, W. A. Hofer, and

Optics EXPRESS

G. Thornton, "Electron traps and their effect on the surface chemistry of TiO_2(110)," Proc. Natl. Acad. Sci. U.S.A. **107**(6), 2391–2396 (2010).
32. M. A. Henderson, W. S. Epling, C. H. F. Peden, and C. L. Perkins, "Insights into photoexcited electron scavenging processes on TiO_2 obtained from studies of the reaction of O_2 with OH groups adsorbed at electronic defects on TiO_2 (110)," J. Phys. Chem. B **107**(2), 534–545 (2003).
33. S. Kashiwaya, J. Morasch, V. Streibel, T. Toupance, W. Jaegermann, and A. Klein, "The work function of TiO_2," Surfaces **1**(1), 73–89 (2018).
34. S. E. Lindquist, B. Finnström, and L. Tegner, "Photoelectrochemical properties of polycrystalline TiO_2 thin film electrodes on quartz substrates," J. Electrochem. Soc. **130**(2), 351–358 (1983).
35. C. Sanchez, K. D. Sieber, and G. A. Somorjai, "The photoelectrochemistry of niobium doped α-Fe_2O_3," J. Electroanal. Chem. **252**(2), 269–290 (1988).
36. D. Tafalla and P. Salvador, "Kinetic approach to the photocurrent transients in water photoelectrolysis at n-TiO_2 electrodes," J. Electrochem. Soc. **137**(6), 1810–1815 (1990).
37. M. Kong, Y. Li, X. Chen, T. Tian, P. Fang, F. Zheng, and X. Zhao, "Tuning the relative concentration ratio of bulk defects to surface defects in TiO_2 nanocrystals leads to high photocatalytic efficiency," J. Am. Chem. Soc. **133**(41), 16414–16417 (2011).
38. R. C. Rai, "Analysis of the Urbach tails in absorption spectra of undoped ZnO thin films," J. Appl. Phys. **113**(15), 153508 (2013).
39. T. Gu, "Role of oxygen vacancies in TiO_2-based resistive switches," J. Appl. Phys. **113**(3), 033707 (2013).